Geolocation of Vacant Bands for Dynamic Spectrum Access via Non-Cooperative Spectrum Sensing

Alfredo Jesús Arbolaez Fundora, Luiz Gustavo Barros Guedes and Dayan Adionel Guimarães

***Abstract*— Accurate geolocation of vacant bands is an essential metric to timely and secure channel use in dynamic spectrum access systems. Non-cooperative spectrum sensing (NCSS) offers a promising solution by directly linking sensing decisions to sensor locations. This study employs NCSS within a database-driven internet of things framework, where scattered sensors perform individual detections and their positions are gathered via Voronoi-based spatial interpolation. Results show that high geolocation accuracy and low variance can be achieved even under unfavorable propagation conditions, supporting efficient and reliable spectrum use.**

***Keywords*— Dynamic spectrum access, spectrum sensing, spectrum hole geolocation, internet of things.**

I. INTRODUCTION

The limited availability of radio frequency spectrum, particularly in wireless systems, represents a significant impediment to the implementation of diverse telecommunications services. This phenomenon can be attributed to the prevailing fixed allocation policy, which confers exclusive access to specific frequencies to designated primary users (PUs). This scenario may lead to spectrum underutilization by PUs or scarcity due to limited availability of new bands. The increasing demand for advanced services, driven by the evolution of fifth-generation (5G) networks, the proliferation of the internet of things (IoT), and the anticipated deployment of sixth-generation (6G) technologies, underscores the pressing need for more efficient spectrum utilization [1], [2].

To effectively implement these technologies, it is necessary to move beyond the fixed spectrum allocation model. Dynamic spectrum access (DSA) schemes have been put forth as a potential solution. These schemes allow secondary networks to exploit underutilized frequency bands without causing interference by strategically accessing available spectrum [3].

In this framework, cognitive radio is presented as a pivotal technology for implementing DSA, allowing for the opportunistic access of free bands. These systems adapt their behavior according to the environment through autonomous and intelligent processes [4].

Alfredo Jesús Arbolaez Fundora, Luiz Gustavo Barros Guedes and Dayan Adionel Guimarães are with the National Institute of Telecommunications (Inatel), Santa Rita do Sapucaí, MG, Brazil (e-mails: alfredo.fundora@mtel.inatel.br; {dayan; luizgustavo.barros}@inatel.br). This work was funded by resources from the following agencies: RNP/MCTI (Grant 01245.010604/2020-14), EMBRAPII/MCTI (Grants 052/2023 PPI IoT/Manufatura 4.0, PPE-00124-23, and Master degree scholarship), FAPESP (Grants 22/09319-9, 20/05127-2), FAPEMIG (Grants APQ-04523-23, APQ-05305-23, APQ-01558-24, RED-00194-23), and CNPq (Grant 302589/2021-0).

Spectrum sensing, one of the key techniques enabled by cognitive radio, seeks to discriminate between two hypotheses in the sensed frequency band by formulating a binary hypothesis test: $\mathcal{H}_0$, which indicates the absence of the PU signal, and $\mathcal{H}_1$, which indicates its presence. This process is evaluated using two basic metrics: probability of detection, P_{d}, and probability of false alarm, P_{fa}. P_{d} measures how effective the spectrum sensing algorithm is at correctly detecting a signal when $\mathcal{H}_1$ is true, while P_{fa} indicates the probability of making a mistake in deciding $\mathcal{H}_1$ when $\mathcal{H}_0$ is actually true. An algorithm is considered optimal if it maximizes P_{d} for a given value of P_{fa} using a fixed number of samples [5].

In spectrum hole geolocation (SHG), binary decisions, i.e. $\mathcal{H}_0$ or $\mathcal{H}_1$, from spectrum sensing are fundamental. Spectrum holes arise when the PU transmitter is inactive or in shadowed regions within its coverage area. The spectrum hole geolocation detection rate (SHGDR) is used to assess accuracy, not as a probability of detection, but as the percentage of correct matches between actual and estimated SHG across the coverage area.

The accuracy of this metric depends on the sensing scheme adopted. In some settings of cooperative spectrum sensing (CSS), multiple distributed secondary users (SUs) share their local observations and apply decision fusion, which helps mitigate propagation effects such as shadowing and fading, thereby increasing detection reliability. However, this cooperation comes at the cost of spatial precision, as the geographic dispersion of the sensing nodes reduces the accuracy in locating spectrum holes. Conversely, non-cooperative spectrum sensing (NCSS) involves individual sensing and decision by each SU. Although the NCSS is more susceptible to the aforementioned propagation phenomena, which may hinder the detection of PU signals in certain areas and potentially result in interference when a PU reoccupies a frequency band mistakenly deemed vacant, this spectrum sensing scheme enables a direct correspondence between the sensing decision and the physical location of the sensor, thereby ensuring more accurate geolocation of spectrum holes [6].

In contrast to approaches based on CSS, such as the one proposed in [6] the present work focuses exclusively on NCSS, where each SSIoT node performs autonomous sensing without information exchange. This individual sensing is integrated into a database-driven DSA framework, with the objective of analyzing the geospatial accuracy in spectrum hole estimation without resorting to cooperative mechanisms. In this manner, the feasibility of NCSS in the construction of spectrum availability maps from local and sparse decisions is studied, and its impact on metrics such as the spectrum hole geolocation detection rate is evaluated.

A. Related Work, Contributions and Paper Structure

Although CSS improves detection reliability, some studies have identified limitations that affect its spatial accuracy. As noted in [7], cooperation may lose effectiveness under spatially correlated shadowing, leading to redundant observations. Moreover, issues such as sensing delay, decision latency, high energy consumption, and vulnerability to attacks further compromise performance.

To mitigate these challenges, database-driven approaches have been incorporated into regulatory standards like IEEE 802.22 [8] and IEEE 802.11af [9], allowing SUs to query spectrum availability based on their location [6]. However, the accuracy of these databases depends on prediction models that often fail to reflect real-time conditions [10].

A hybrid alternative is reviewed in [11], combining sensing and databases via IoT-based spectrum sensors (SSIoTs), which periodically update the database and offload sensing from SUs. This approach, adopted in [6], supports spectrum hole geolocation through overlapping clustering and enhances sharing efficiency.

In contrast to the extensive attention received by CSS, NCSS has been less explored as a viable alternative for SHG. Despite the existence of proposals that employ energy sensing, cyclostationary techniques, or deep learning methods, the majority of these have focused on the analysis of global sensing metrics as P_{d} and P_{fa} without explicitly addressing the construction of spatial maps of spectrum availability.

The present study proposes, as its main contribution, an alternative solution that employs the NCSS approach and is predicated on the spatial interpolation of individual node decisions, within the same conceptual framework proposed in [11] and utilized in [6], with the distinctive feature of entirely eliminating inter-node cooperation, a characteristic that is not only coherent with the nature of non-cooperative sensing, but also removes the need for data exchange or decision fusion among nodes, thereby simplifying implementation and reducing communication overhead.

The remainder of this paper is organized as follows: Section II describes the system model adopted in this work. Section III details the proposed SHG method. Section IV presents the numerical results, including SHG performance metrics under different configurations. Finally, Section V draws conclusions and outlines directions for future research.

II. System Model

This section delineates the models employed to represent the transmitted and received signals, the noise, the sensing channel, and the detection technique, which have been selected on the basis of their realism and suitability to practical scenarios. Subsequent to the non-cooperative approach, models inspired by those presented in [12], which are widely recognized in the context of spectrum sensing, are employed.

We consider a network composed of N_1 SSIoTs, randomly distributed over a square region of side L. Each SSIoT performs spectrum sensing individually, without exchanging information with other nodes. At each sensing interval, the signal received by the i-th SSIoT, $\mathbf{y}_i \in \mathbb{C}^{n\times 1}$, is modeled as

$$\mathbf{y}_i = h_i \mathbf{x}^{\mathrm{T}} + \mathbf{v}_i \tag{1}$$

where $\mathbf{x} \in \mathbb{C}^{n\times 1}$ is the PU signal transmitted vector. The complex samples vector of the PU signal is generated as a QPSK sequence with oversampling, such that the samples exhibit non-zero correlation due to the temporal redundancy introduced. $h_i \in \mathbb{C}$ is the channel gain between the PU and the i-th SSIoT, and $\mathbf{v}_i \in \mathbb{C}^{n\times 1}$ represents thermal noise, modeled as additive white Gaussian noise (AWGN).

The channel h_i captures the propagation effects and is modeled as

$$h_i = G_i a_i \tag{2}$$

where a_i represents the multipath fading component and G_i is the local mean gain that accounts for distance-dependent path-loss and shadowing. The fading component a_i is assumed to follow a Rician distribution, in which the Rice factor K_{ij} is modeled as a Gaussian random variable with mean μ_K and standard deviation σ_K, both in dB and dependent on the propagation environment. According to experimental findings reported in [13], urban areas typically exhibit $\mu_K = 1.88$ dB and $\sigma_K = 4.13$ dB. This formulation enables a realistic representation of the propagation conditions in dynamic wireless environments.

The gain G_i is defined based on the average received signal power $P_{r,i}$ as

$$G_i = \sqrt{\frac{P_{r,i}}{P_t}} \tag{3}$$

where P_t is the PU transmission power. The expression for $P_{r,i}$, in dBm, follows a path-loss model with log-normal shadowing, proposed in [14], as

$$P_{r,i}^{\mathrm{dBm}} = 10\log_{10}\left(10^3 P_t \left(\frac{d_0}{d_i}\right)^{\eta}\right) + S_i, \tag{4}$$

so that d_i is the distance between i-th node and the PU transmitter, d_0 is a reference distance, η is the path-loss exponent, and S_i is a random variable representing log-normal shadowing with spatial correlation, as described in [15]. To model long-term signal variations caused by environmental obstructions, the shadowing term S_i is defined as a spatially correlated log-normal variable. Based on the exponential decay function of Euclidean distance and the spatial correlation parameter λ, a correlation matrix is built following the method in [16]. Correlated shadowing values are then generated by applying Cholesky decomposition to this matrix and multiplying it by a vector of independent and identically distributed standard Gaussian variables, assigning each node i its value S_i according to its location. This model provides a realistic spatial distribution of signal attenuation and supports the simulation of coverage irregularities, such as spectrum holes caused by the propagation environment.

In practice, thermal noise levels are not uniform due to environmental and hardware-related variations. Thus, the noise variance at i-th node is modeled as a random variable fluctuating around the average value $\bar{\sigma}^2$, given by

$$\sigma_{v_i}^2 = (1 + \zeta u_i)\,\bar{\sigma}^2 \tag{5}$$

where $u_i \sim \mathcal{U}[-1, 1]$ and $\zeta \in [0, 1)$ controls the degree of variability. This model accounts for realistic noise differences across devices.

Since both the received signal power and the noise level may vary across nodes, an average link quality metric is defined using the expected signal-to-noise ratio (SNR). It is computed as the product of the expected received power and the expected inverse of the noise variance given by

$$\text{SNR} = \mathbb{E}[P_{r,i}] \cdot \mathbb{E}\left[\frac{1}{\sigma_{v_i}^2}\right] \tag{6}$$

This global metric characterizes the average system performance and enables comparison between different sensing strategies under statistically equivalent conditions.

A. Sample Covariance Matrix and Pietra-Ricci index Detector

As the proposed scheme relies on a single vector of n samples per node, this vector is first centered by subtracting its mean. Then, it is divided into $K = n/M$ consecutive non-overlapping segments of equal length M, where M denotes the desired order of the sample covariance matrix (SCM). Each of these segments represents a portion of the original vector and is used to estimate the local SCM at node i, which is given by

$$\mathbf{R}_i = \frac{1}{K}\sum_{k=1}^{K} \mathbf{z}_{i,k}^T \mathbf{z}_{i,k}, \tag{7}$$

where $\mathbf{z}_{i,k} \in \mathbb{C}^{M\times 1}$ denotes the k-th segment of the centered vector. This procedure allows for a robust estimation of the SCM from a single observation vector, preserving the statistical structure required for the subsequent computation of the decision statistic.

Once the covariance matrix $\mathbf{R}_i$ is estimated, the Pietra-Ricci Index Detector (PRIDe) is used to make a local decision at i-th node, due to its effectiveness in terms of performance, complexity, and latency [17], [18], [19].

Let $r_{i,z,k}$ denote the (z, k)-th entry of $\mathbf{R}_i$, for $z, k = 1, \ldots, M$. The average entry of the matrix is defined as

$$\bar{r}_i = \frac{1}{M^2}\sum_{z=1}^{M}\sum_{k=1}^{M} r_{i,z,k}. \tag{8}$$

The PRIDe test statistic for i-th node is given by:

$$T_{\text{PRIDe},i} = \frac{\sum_{z=1}^{M}\sum_{k=1}^{M} |r_{i,z,k}|}{\sum_{z=1}^{M}\sum_{k=1}^{M} |r_{i,z,k} - \bar{r}_i|}. \tag{9}$$

A decision regarding the occupation status of the sensed band is made by comparing $T_{\text{PRIDe},i}$ against a threshold γ_i associated with a predefined P_{fa}. If $T_{\text{PRIDe},i} > \gamma_i$, the presence of a PU signal in the sensed band is declared; otherwise, the band is considered free.

III. Proposed Method

The proposed method utilizes a NCSS strategy to perform SHG. In this strategy, each spectrum sensing device makes local decisions. The PRIDe detector is used to determine the presence or absence of the primary signal in the sensed band.

Subsequent to the issuance of a binary decision by each node, an association is established between the node and its geographic position within the sensing area. A spatial map of spectrum occupancy is created from these individual decisions. In order to achieve this, the designated area is divided into discrete regions using a Voronoi diagram, where each region is connected to the closest node based on the Euclidean distance principle. The decision made by a given node is assigned to the entire region to which it belongs. Consequently, a binary map is generated that differentiates between occupied and unoccupied areas, based on the local decisions of the SSIoTs. Furthermore, an interpolation logic is implemented to enhance the spatial representation. In particular, if there are pairs of nearby nodes that do not detect signal and meet a proximity condition defined by a distance threshold, the intermediate region is also considered to correspond to a spectrum hole.

Figure 1 presents, for instance, the spatial results obtained in one round of sensing. Fig. 1a, illustrates the distribution of the actual SHG, which are generated from the received power threshold under realistic propagation conditions. Fig. 1b, shows the estimated SHG map without interpolation, where each Voronoi cell is directly colored according to the local decision of the corresponding sensor. Fig. 1c presents the estimated map with interpolation applied, in which nearby undetected regions are grouped as spectrum holes, while isolated cells are treated differentially to reduce interpolation errors.

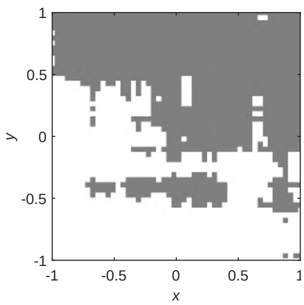

(a) Snapshot of actual SHG.

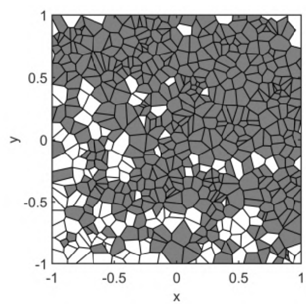

(b) Corresponding estimated SHGs.

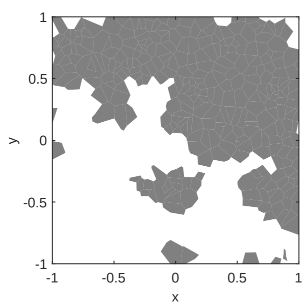

(c) Corresponding interpolated SHGs.

Fig. 1. Example of spatial results considering 600 scattered SSIoT devices.

The efficacy of the method depends on the chosen configuration parameters. Sensor density impacts the spatial resolution and effective area coverage. The interpolation threshold distance is related to the system's ability to detect spectrum holes between nearby nodes. The SCM order M significantly affects the accuracy and stability of the local PRIDe statistic. Additionally, the SNR directly influences the reliability of individual decisions, while the decision threshold defines the detector's sensitivity and can greatly affect map quality.

This approach, predicated exclusively on individual decisions and devoid of information exchange between nodes, facilitates a scalable and efficient implementation in dense and dynamic IoT networks.

IV. Numerical Results

The parameters utilized in the simulations are enumerated in Table 1, and the codes used are provided in [20]. Here, a square scenario was considered, in which the SSIoTs were randomly distributed. Furthermore, a distance threshold is utilized in the spatial interpolation process via the implementation of Voronoi diagrams. The construction of the SCMs is executed from subsets of observed samples, with the objective of ensuring the estimation of the PRIDe test statistic is robust.

TABLE I. Main default system parameters.

Parameter	Value
Total number of SSIoTs in the basis network, N_1	500
Fraction of fixed SSIoT nodes, α	0.5
Side length of the coverage area, L	9000 m
Signal-to-noise ratio, SNR	-5 dB
Noise variability factor, ρ	0.5
Number of sensing rounds	10000
Samples per SSIoT, n	1500
Path-loss exponent, η	2.5
Reference distance for path-loss, d_0	0.1 m
Transmitter power, P_t	5 W
PU location, $(x_{\text{PU}}, y_{\text{PU}})$	$(2L, 2L)$ m
Mean of the Rice factor, $\bar{K}$	1.88 dB
Standard deviation of Rice factor, σ_K	4.13 dB
Shadowing std. deviation, σ_s	7 dB
Correlation length of shadowing, Λ	0.8× rows
Order of the covariance matrix, M	15
Threshold for spectrum hole, $P_{\text{rx,th}}$	-100 dBm
Distance threshold for interpolation, d_{thresh}	$4/\sqrt{N_1/L^2}$
Probability of false alarm, P_{fa}	0.2

Figure 2 illustrates the SHGDR distribution obtained using the same configuration of 500 sensors as in Fig. 10 of [6], where a CSS scheme based on overlapped clusters is employed. This alignment enables a direct comparison between the two approaches. In the proposed NCSS framework, the mean SHGDR reached approximately 0.772, with a variance of 0.0054, indicating a broader dispersion relative to the cooperative method, which achieved a higher mean SHGDR of approximately 0.85 and a variance around 0.005. While the CSS approach leverages spatial cooperation to mitigate propagation effects and enhance detection accuracy, it also introduces spatial ambiguity in spectrum hole geolocation due to the aggregation of sensing data across clusters. In contrast, the NCSS method maintains spatial fidelity by directly associating detections with sensor locations, albeit with increased variability in detection outcomes. This distinction underscores the inherent trade-off: CSS enhances detection consistency at the expense of spatial precision, whereas NCSS preserves location-specific accuracy but incurs higher variance. As demonstrated in the subsequent analysis, increasing sensor density in the NCSS framework can potentially bridge the detection gap while sustaining spatial alignment, highlighting its scalability in dense IoT scenarios.

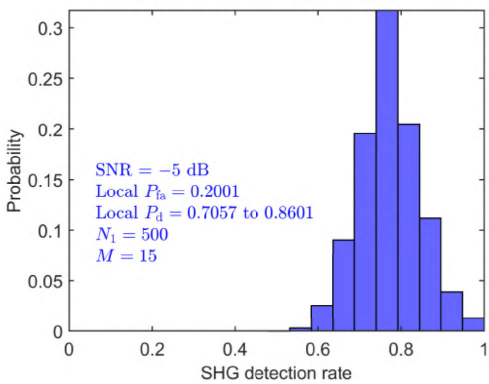

Fig. 2. Histogram of the spectrum hole geolocation detection rate.

Fig. 3 presents the behavior of the SHGDR as a function of the total number of SSIoTs, N_1, while keeping the remaining parameters shown in Table I constant. The mean SHGDR has been found to maintain relative stability with values between 75% and 80%, suggesting a strong performance of the NCSS scheme. As evidenced at the base of the figure and similarly noted in Fig. 13 of [6], increasing the number of sensors N_1 leads to a gradual decrease in variance. Concurrently, the SHGDR shows slight improvement and tends to stabilize as N_1 grows. This behavior reinforces the idea that greater node density can enhance spatial accuracy, although with diminishing returns beyond a certain threshold.

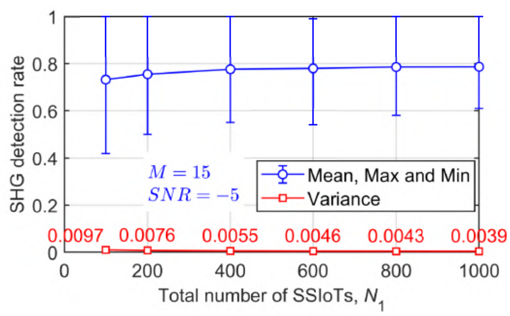

Fig. 3. SHGDR versus the total number of SSIoTs, N_1.

Fig. 4 shows the behavior of the SHGDR as a function of the SNR. Similar to Fig. 11 in [6], the average SHGDR exhibits a noticeable increase as the SNR improves, ranging from approximately 50% at -15 dB to nearly 79.3% at -3 dB. This trend confirms the robustness of the NCSS scheme across a wide range of noise conditions. Despite some fluctuations, the variance values remain relatively low, and the gap between maximum and minimum SHGDR tends to narrow, indicating more consistent decision-making in such conditions.

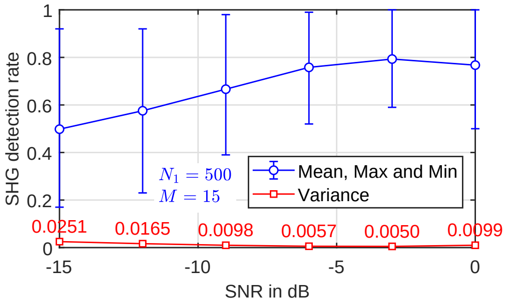

Fig. 4. SHGDR versus SNR.

Although, under identical conditions, the CSS scheme based on overlapping clusters shows slightly superior performance, by properly adjusting the operating parameters it is possible to largely match the SHGDR of the proposed method. In this way, a precision comparable to that obtained in [6] is achieved, with the advantage of a much simpler deployment and a less complex architecture.

V. Conclusions

The present paper put forth an alternative strategy for geolocating spectrum holes in DSA systems. This strategy is based exclusively on NCSS within a database-driven IoT framework. The proposal's elimination of sensor cooperation results in a reduction of complexity, energy consumption, and latency without compromising spatial accuracy. The simulation experiment yielded results that demonstrated the efficacy of the method under investigation. Specifically, the experiment incorporated various configurations of sensors and different SNRs. The results of the simulation experiment demonstrated robust performance, characterized by satisfactory average detection rates and low variance. These outcomes serve to validate the effectiveness of the method employed.

While CSS generally offers superior detection performance due to diversity and collaboration, NCSS can be a better choice in certain situations. NCSS is advantageous when CSS suffers from spatially-correlated shadowing, high mobility, or when rapid decisions are needed, as it avoids delays from coordination and fusion. It also offers improved robustness in networks with unreliable or malicious nodes and reduces security and privacy risks by keeping data local. Overall, the simplicity and independence of NCSS make it preferable in specific challenging environments where CSS performance degrades or complexity is a limiting factor.

Subsequent studies will entail the implementation of machine learning methodologies to enhance the spatial interpolation of individual decisions, in addition to the integration of adaptive mechanisms to dynamically adjust the system parameters according to the environment. This solution signifies a substantial advancement in the direction of more straightforward and extensible architectures for SHG in IoT networks.

References

[1] A. Nasser, H. Al Haj Hassan, J. Abou Chaaya, A. Mansour, and K.-C. Yao, "Spectrum sensing for cognitive radio: Recent advances and future challenge," *Sensors*, vol. 21, no. 7, 2021. [Online]. Available: https://www.mdpi.com/1424-8220/21/7/2408

[2] W. Dias, A. Ferreira, R. Kagami, J. S. Ferreira, D. Silva, and L. Mendes, "5g-range: A transceiver for remote areas based on software-defined radio," in *2020 European Conference on Networks and Communications (EuCNC)*, 2020, pp. 100–104.

[3] U. S. F. C. C. S. P. T. Force, *Report*. Federal Communications Commission, Spectrum Policy Task Force, 2002. [Online]. Available: https://books.google.com.br/books?id=p9MQtwAACAAJ

[4] M. R. Manesh, M. S. Apu, N. Kaabouch, and W.-C. Hu, "Performance evaluation of spectrum sensing techniques for cognitive radio systems," in *2016 IEEE 7th Annual Ubiquitous Computing, Electronics Mobile Communication Conference (UEMCON)*, 2016, pp. 1–7.

[5] Y. Zeng, Y.-C. Liang, A. T. Hoang, and R. Zhang, "A review on spectrum sensing for cognitive radio: Challenges and solutions," *EURASIP Journal on Advances in Signal Processing*, vol. 2010, no. 1, 2010. [Online]. Available: https://doi.org/10.1155/2010/381465

[6] D. A. Guimarães, "Spectrum hole geolocation for database-driven iot-enabled dynamic spectrum access," *IEEE Access*, vol. 13, pp. 64 199–64 215, 2025.

[7] I. F. Akyildiz, B. F. Lo, and R. Balakrishnan, "Cooperative spectrum sensing in cognitive radio networks: A survey," *Physical Communication*, vol. 4, no. 1, pp. 40–62, 2011. [Online]. Available: https://www.sciencedirect.com/science/article/pii/S187449071000039X

[8] "Ieee standard for information technology– local and metropolitan area networks– specific requirements– part 22: Cognitive wireless ran medium access control (mac) and physical layer (phy) specifications: Policies and procedures for operation in the tv bands," *IEEE Std 802.22-2011*, pp. 1–680, 2011.

[9] "Iso/iec/ieee international standard – information technology – telecommunications and information exchange between systems – local and metropolitan area networks – specific requirements – part 11: Wireless lan medium access control (mac) and physical layer (phy) specifications amendment 5," *ISO/IEC/IEEE 8802-11:2012/Amd.5:2015(E) (Adoption of IEEE Std 802.11af-2014)*, pp. 1–204, 2015.

[10] Z. Qin, Y. Gao, and C. G. Parini, "Data-assisted low complexity compressive spectrum sensing on real-time signals under sub-nyquist rate," *IEEE Transactions on Wireless Communications*, vol. 15, no. 2, pp. 1174–1185, 2016.

[11] D. A. Guimarães, E. J. T. Pereira, A. M. Alberti, and J. V. Moreira, "Design guidelines for database-driven internet of things-enabled dynamic spectrum access," *Sensors*, vol. 21, no. 9, 2021. [Online]. Available: https://www.mdpi.com/1424-8220/21/9/3194

[12] D. A. Guimarães, "Hybrid fusion of pietra–ricci index detector information for cooperative spectrum sensing," *Ad Hoc Networks*, vol. 150, p. 103265, 2023. [Online]. Available: https://www.sciencedirect.com/science/article/pii/S1570870523001853

[13] S. Zhu, T. S. Ghazaany, S. M. R. Jones, R. A. Abd-Alhameed, J. M. Noras, T. Van Buren, J. Wilson, T. Suggett, and S. Marker, "Probability distribution of rician k-factor in urban, suburban and rural areas using real-world captured data," *IEEE Transactions on Antennas and Propagation*, vol. 62, no. 7, pp. 3835–3839, 2014.

[14] T. Rappaport, *Wireless Communications: Principles and Practice*, 2nd ed. USA: Prentice Hall PTR, 2001.

[15] J. M. Vallet García, "Characterization of the log-normal model for received signal strength measurements in real wireless sensor networks," *Journal of Sensor and Actuator Networks*, vol. 9, no. 1, 2020. [Online]. Available: https://www.mdpi.com/2224-2708/9/1/12

[16] M. Gudmundson, "Correlation model for shadow fading in mobile radio systems," *Electronics Letters*, vol. 27, no. 23, pp. 2145–2146, November 1991.

[17] D. A. Guimarães, "Pietra-ricci index detector for centralized data fusion cooperative spectrum sensing," *IEEE Transactions on Vehicular Technology*, vol. 69, no. 10, pp. 12 354–12 358, 2020.

[18] D. A. Guimarães, E. J. T. Pereira, and R. Shrestha, "Resource-efficient low-latency modified pietra-ricci index detector for spectrum sensing in cognitive radio networks," *IEEE Transactions on Vehicular Technology*, vol. 72, no. 9, pp. 11 898–11 912, 2023.

[19] E. J. T. Pereira, D. A. Guimarães, and R. Shrestha, "Vlsi architectures and hardware implementation of ultra low-latency and area-efficient pietra-ricci index detector for spectrum sensing," *IEEE Transactions on Circuits and Systems I: Regular Papers*, vol. 71, no. 5, pp. 2348–2361, 2024.

[20] A. J. Arbolaez Fundora, "Simulation codes: *Codes* folder in "simulation-codes" repository," https://github.com/Alfre2AF/Simulation-codes/tree/main/Codes, 2025, accessed: July 12, 2025.